Northumbria Research Link

Chao Mei [a], Jinhui Yuan [a, b, *], Feng Li [b, c, *], Binbin Yan [a], Xinzhu Sang [a], Xian Zhou [d], Qiang Wu [e], Kuiru Wang [a], Keping Long [d], and Chongxiu Yu [a]

Generation of parabolic pulse in a dispersion and nonlinearity jointly engineered silicon waveguide taper

[a] State Key Laboratory of Information Photonics and Optical Communications, Beijing University of Posts and Telecommunications, Beijing, China
[b] Photonics Research Centre, Department of Electronic and Information Engineering, The Hong Kong Polytechnic University, Hong Kong SAR, China
[c] The Hong Kong Polytechnic University Shenzhen Research Institute, Shenzhen 518057, China
[d] Research Center for Convergence Networks and Ubiquitous Services, University of Science & Technology Beijing (USTB), Beijing 100083, P. R. China.
[e] Department of Physics and Electrical Engineering, Northumbria University, Newcastle upon Tyne, NE1 8ST, United Kingdom
*Corresponding author: yuanjinhui81@bupt.edu.cn, enlf@polyu.edu.hk

Abstract: In this paper, we numerically investigate the generation of parabolic pulse (PP) in a silicon waveguide taper with simultaneous variations of the group-velocity dispersion and nonlinearity along the propagation direction. The design of such a waveguide taper is based on the condition of self-similar propagation of the PP. When Gaussian, hyperbolic secant, and super-Gaussian pulses are propagated inside the waveguide taper designed, the evolution processes under the ideal condition are analyzed. Then the PP generation from Gaussian input is shown when higher-order dispersion, higher-order nonlinearity, linear loss, two-photon absorption, free-carrier absorption, and free-carrier dispersion are taken into account. Moreover, the influences of the initial chirp, pulse width, peak power, and waveguide length on the PP generation are further discussed. It is demonstrated that high-quality PP can be obtained with a mismatch parameter as low as 1.3×10^{-3} in the designed silicon waveguide taper.

Keywords: *parabolic pulse; silicon waveguide; self-similar theory*

1. Introduction

Parabolic pulse (PP) represents a class of optical pulses that are wave-breaking free in the presence of group-velocity dispersion (GVD) and nonlinearity [1]. Recently, the PP has been attracting much interest because of its important applications in high power amplifiers [2], ultrashort pulse generation [3], etc. Generally speaking, the PP can be asymptotically generated in optical fiber amplifiers with normal dispersion profile [4], where the fiber gain plays a key role on providing excessive nonlinear phase accumulation for the pulse shaping. Theoretical analysis has proved that an equivalent gain can be obtained in passive tapered nonlinear media [5], where the influence of the spontaneous emission noise amplified in active nonlinear media can be avoided. Several schemes on the PP generation in passive optical fiber tapers have been reported [6, 7]. With the development of on-chip integrated optical devices, recent works are focused on the PP generation in integratable silicon photonic wire [8]. However, the intrinsic two-photon absorption (TPA) and free-carrier absorption (FCA) in silicon material have detrimental influences on the PP generation. Theoretically, the PP generation is an asymptotic process, which obeys the self-similar rules. Thus, it is necessary to investigate the waveguide design based on the condition of self-similarity. In our previous work, the PP generation in the amorphous silicon waveguide tapers designed with respectively hyperbolically decreasing GVD or exponentially increasing

nonlinearity is reported [9]. However, in the actual situation, a waveguide taper with single changing GVD or nonlinearity is hard to achieve because they both vary with the waveguide width. Up to now, there is still no report on the exact waveguide design with simultaneous variations of the GVD and nonlinearity for the PP generation.

In this paper, we report the generation of the PP in silicon waveguide taper with simultaneous variations of the GVD and nonlinearity. Different from previous work in which the passive waveguide tapers for PP generation are designed without considering the relation between GVD and nonlinearity, here we construct the relation of GVD and nonlinearity and then design the silicon waveguide taper by using the bisection method. In this newly designed waveguide, we consider the pulse evolution to PP with the input of super-Gaussian, Gaussian and hyperbolic secant profiles. Moreover, we consider the effects of higher-order dispersion (HOD), higher-order nonlinearity (HON), linear loss, TPA, FCA, and free-carrier dispersion (FCD) in the designed silicon waveguide taper. The influences of the initial chirp, pulse width, peak power, and waveguide length are also studied.

2. Theoretical model

We start from the variable-coefficients nonlinear Schrödinger equation (NLSE) with the linear loss term as following

$$A_z = -iD_0\theta(z)A_{tt} + i\gamma_0\varepsilon(z)|A|^2 A - \rho_0\eta(z)A, \qquad (1)$$

where $A(z, t)$ is the slow-varying envelop of the electric field, and z and t are the propagation distance and retarded time. $D_0 = \beta_2(0)/2$, γ_0, and $\rho_0 = \alpha(0)/2$ are the initial values of the GVD, nonlinear coefficient, and linear loss, respectively. $\theta(z)$, $\varepsilon(z)$, and $\eta(z)$ describes the normalized variations of the GVD, nonlinearity, and linear loss. For the waveguide with a normal dispersion profile, where $D_0 > 0$ and $\theta(z) > 0$, we define

$$\kappa(z) = \int_0^z \theta(x)dx, \qquad (2)$$

where $\kappa(z)$ is a monotonic function and there is an inverse function $z(\kappa)$, then Eq. (1) can be written as

$$A_\kappa = -iD_0 A_{tt} + i\gamma_0 \frac{\overline{\varepsilon}(\kappa)}{\overline{\theta}(\kappa)}|A|^2 A - \rho_0 \frac{\overline{\eta}(\kappa)}{\overline{\theta}(\kappa)}A, \qquad (3)$$

To transform Eq. (3) into the form of NLSE with the gain, we define

$$A = a(\kappa)u, \qquad (4)$$

Substituting Eq. (4) into Eq. (3), we have

$$u_\kappa = -iD_0 u_{tt} + i\frac{\gamma_0 a^2(\kappa)\bar{\varepsilon}(\kappa)}{\bar{\theta}(\kappa)}|u|^2 u - \left[\frac{\rho_0\bar{\eta}(\kappa)}{\bar{\theta}(\kappa)} + \frac{a'(\kappa)}{a(\kappa)}\right]u. \quad (5)$$

A constant gain can be obtained if

$$\left[\frac{\rho_0\bar{\eta}(\kappa)}{\bar{\theta}(\kappa)} + \frac{a'(\kappa)}{a(\kappa)}\right] = \frac{g}{2}, \quad (6)$$

where g is a constant determined by the waveguide taper profile. To support the self-similar propagation of the PP, we have

$$\frac{a^2(\kappa)\bar{\varepsilon}(\kappa)}{\bar{\theta}(\kappa)} = 1, \quad (7)$$

Combining Eq. (6) and Eq. (7), we have

$$\bar{\varepsilon}(\kappa) = \bar{\theta}(\kappa)\exp\left(g\kappa + 2\rho_0\bar{\eta}(\kappa)\int_0^\kappa \frac{1}{\bar{\theta}(\kappa')}d\kappa'\right), \quad (8)$$

Now we return to the scale with z and Eq. (8) is written as

$$\varepsilon(z) = \theta(z)\exp\left(g\int_0^z \theta(z')dz' + 2\rho_0\int_0^z \eta(z')dz'\right). \quad (9)$$

Thus, the relation between the nonlinearity and GVD can be described as

$$\gamma(z) = \frac{\gamma_0\beta_2(z)}{\beta_0}\exp\left[g\int_0^z \varepsilon(z')dz' + 2\rho_0\int_0^z \eta(z')dz'\right]. \quad (10)$$

Eq. (10) is the condition of self-similarity to guarantee the design of a waveguide with simultaneous variations of the GVD, nonlinearity for generating a PP. $g(z)$ is an equivalent gain given as

$$g = \frac{\ln\left[\varepsilon(z)/\theta(z)\right] - 2\rho_0\int_0^z \eta(z')dz'}{\int_0^z \theta(z')dz'}. \quad (11)$$

We can see that the value of g is determined by $\varepsilon(z)$, $\theta(z)$, ρ_0, and $\eta(z)$. If the linear loss is assumed to be a constant, namely $\eta(z) = 1$, the solution of Eq. (1) is

$$A(z,t) = \sqrt{P(z)}\left[1 - 2t^2/t_F^2\right]^{1/2}\exp\left[\phi(z,t)\right], \quad (12)$$

where $P(z)$ is the peak power, t_F is the full width at half maximum (FWHM), and $\phi(z, t)$ is the phase whose initial value is assumed to be zero. By adopting the self-similar technique [10], we finally obtain $P(z)$ as

$$P(z) = \frac{(gE_0)^{2/3}}{4}\left(\frac{1}{\gamma_0 D_0}\right)^{1/3}\frac{\theta(z)}{\varepsilon(z)}\exp\left[\frac{2}{3}g\int_0^z \theta(z')dz'\right], \quad (13)$$

where E_0 is the energy of input pulse. The solutions of the pulse width and phase terms are given as

$$t_F = 3\sqrt{2}\left(\frac{E_0\gamma_0 D_0}{g^2}\right)^{1/3}\frac{\varepsilon(z)}{\theta(z)}\exp\left[\frac{-2g}{3}\int_0^z \theta(z')dz' - 2\rho_0 z\right], \quad (14)$$

$$\phi(z,t) = \frac{3}{8}\left(\frac{\gamma_0 E_0}{g^2\sqrt{D_0}}\right)^{2/3}\exp\left(\frac{2g}{3}\int_0^z \theta(z')dz'\right) - \frac{g}{12D_0}t^2. \quad (15)$$

It can be seen from Eqs. (13)-(15) that $P(z)$, $t_F(z)$, and $\phi(z, t)$ are jointly determined by E_0, D_0, γ_0, $\theta(z)$, $\varepsilon(z)$, and ρ_0. Compared with the active fibers where the PP generation only depends on the input energy and intrinsic gain, more parameters can be utilized to control the PP generation in a passive nonlinear taper.

3. Design of the silicon waveguide taper

Based on the condition of self-similarity which indicated by Eq. (10), a passive silicon waveguide taper with constant height

(H) of 220 nm, varying width (W) from 1600 to 800 nm along z and waveguide length of 1 cm is proposed. In order to investigate the variations of the optical field and the confinement loss of the silicon waveguide taper at 1550 nm, the effective mode area A_{eff} and energy ratio E_r are calculated along as functions of the reduction of waveguide width. A_{eff} and E_r can be calculated based on the fundamental mode distribution [11] and E_r is obtained by calculating the ratio of energy flow in the core and cladding regions of the silicon waveguide taper, respectively. The energy flow can be obtained from the integral of the Poynting vector over the whole cross-section. For the TE mode considered, E_r is calculated with the following formula,

$$E_r = \frac{\text{Re}\left(\iint_{core} \overset{\vee}{S}dxdy\right)}{\text{Re}\left(\iint_{cladding} \overset{\vee}{S}dxdy\right)} = \frac{\text{Re}\left(\iint_{core} E_x \times H_y^* dxdy\right)}{\text{Re}\left(\iint_{cladding} E_x \times H_y^* dxdy\right)}, \quad (16)$$

where S is the Poynting vector, E_x and H_y represent the electric field in the x direction and the magnetic field in the y direction, respectively. Re() means the real part of the argument inside the parenthesis. The calculation results are shown in Fig. 1. As the waveguide width decreases, A_{eff} decreases from 0.33 to 0.18 μm^2, and the confinement loss gradually increases, which can be seen from the reduction of E_r. However, the change of E_r is very small. Thus, it is not necessary to consider the energy attenuation caused by the confinement loss during the propagation, which is very meaningful for practical application.
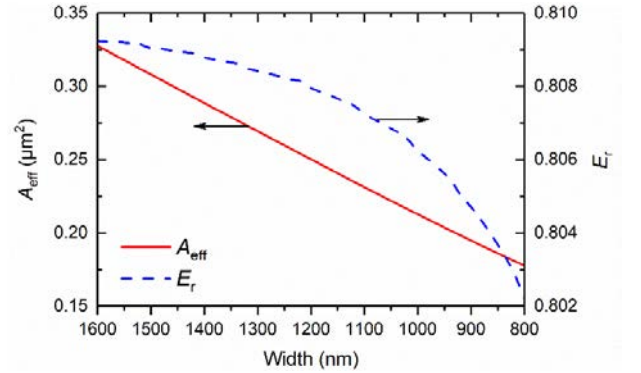

Fig. 1. The variations of effective mode area A_{eff} (red solid curve) and energy ratio E_r (blue dashed curve) as functions of waveguide width.

The finite element method is used to calculate $\beta_2(W)$ and $\gamma(W)$ under different W. Then Eq. (10) is solved to obtain γ once $\beta_2(W)$ is chosen at W, e. g. 1600 nm which corresponds to the propagation distance of $z = 0$. The obtained γ is compared with $\gamma(W)$ at the chosen W. If the difference between them is very small, it is confirmed that β_2, γ, and W at $z = 0$ is found. The determined β_2 and γ satisfy Eq. (10). Thereafter, the values of β_2, γ, and W at $z + \Delta z$ can be also obtained by using the same procedure. After the loop calculation for many times, the relations of β_2, γ, and W between z which is changed from 0 to 1 cm can be finally obtained. In our calculation, ρ_0 is chosen as 0.25 dB/cm. This value is reasonable with current fabrication technology of silicon waveguide [12-15]. In fact, after carefully designing the cross-section of waveguides and optimizing the lithography and dry etching processes, the scattering loss caused by the sidewall roughness can be reduced. In Fig. 2(a), the relations of β_2 and γ between z are fitted by 5-th order polynomials, which satisfy Eq. (10). Figure 2(b) shows the relation between W and z. Insets I and II in Fig. 2(b) show the three-dimensional sketch and cross-section of the proposed silicon waveguide taper. Because of the large refractive index contrast between the Si and SiO$_2$, the optical mode fields can be well confined at the input and output ports of the waveguide

taper. The waveguide taper can support multiple modes. However, in our simulation, we found that the group-velocity difference between the fundamental mode and higher-order modes so large that the walk-off length is much less than the waveguide length. As a result, the higher-order modes have a slight influence on the fundamental mode. Thus, we only consider the pulse evolution of fundamental mode. As W is gradually decreased as z increases and resulting in a smaller mode field area at the output port, γ increases along z, as shown in Fig. 2(a).
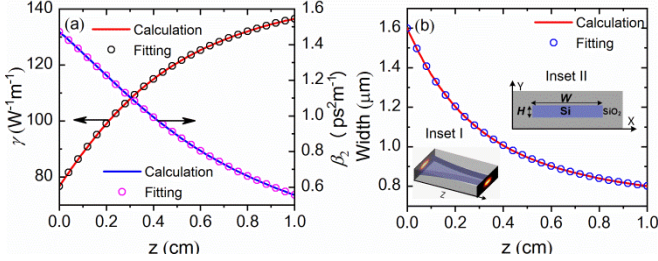

Fig. 2. (a) The variations of β_2 and γ along z, the solid curves are the calculation results with the bisection method, and the hollow circles correspond to the polynomial fitting. (b) The variation of width (W) along z, the solid and hollow curves corresponding to the calculation result with the bisection method and the polynomial fitting, respectively. Insets I and II in (b) show the three-dimensional sketch and cross-section of the silicon waveguide taper, along with the optical field distributions at the input and output ports, respectively.

4. Simulation results and discussion

The peak power, pulse width, and phase of the PP can be theoretically predicted for a certain waveguide taper from Eqs. (13)-(15), as plotted by the black curves in Fig. 3. If the input pulse is not PP, the pulse power, width, and phase would gradually evolve to the theoretical values [4]. To verify the generation of PP from different input profiles, the super-Gaussian pulse, $A(0,t) = (P_0)^{1/2}\exp[-(t/T_0)^{2m}/2]$, the Gaussian pulse, $A(0,t) = (P_0)^{1/2}\exp[-(t/T_0)^2/2]$, and the hyperbolic secant, $A(0,t) = (P_0)^{1/2}\mathrm{sech}(t/T_0)$ are launched into the designed silicon waveguide taper, respectively. The three kinds of pulses have the same E_0 and P_0 of 0.88 pJ and 4 W, respectively. T_0 can be derived from E_0 and P_0. For super-Gaussian pulse, $E_0 = \Gamma(1/2m)T_0P_0/m$ and $m = 2$ in our simulation. For Gaussian pulse, $E_0 = (\pi)^{1/2}T_0P_0$ and for hyperbolic secant pulse, $E_0 = 2T_0P_0$. The corresponding T_0 for the three pulses are 121.3 fs, 124.1 fs and 110 fs. The output pulses are plotted in Fig. 3(a), where the three kinds of pulses are well fitted by the parabolas. But for the super-Gaussian pulse, the deviations at the leading and trailing edges are obvious. In Fig. 3(b), the chirps of the three pulses vary linearly in the center region of the pulse, but the curvatures at the leading and trailing edges of the pulse are different. For Gaussian and hyperbolic secant pulses, the overlap of the chirp at the center region of the pulse with the theoretical curve is not as high as that of the super-Gaussian pulse. However, the chirps of Gaussian and the hyperbolic secant pulses at the leading and trailing edges are not curved severely compared to the super-Gaussian pulse. Therefore, in Fig. 3(c), although the peak powers of the three pulses gradually approach the theoretical curve during the propagation, the evolutionary trajectory of the super-Gaussian pulse is slightly different from those of the other two pulses. At the initial stage, the peak power of the super-Gaussian pulse gradually deviates from the theoretical curve. After the deviation reaching the maximum value, it starts to quickly approach the theoretical curve. Finally, the peak powers of the three pulses are almost the same at the output end of the waveguide taper. As a contrast, the peak powers of the Gaussian

and hyperbolic secant pulses smoothly approach the theoretical curve during the evolution. Root-mean-square (RMS) pulse width [16] is used to characterize the pulse width in the complex pulse reshaping process. The RMS pulse width versus z is plotted in Fig. 3(d). The evolution trajectories of the three pulse shapes can also be seen in this figure. The super-Gaussian pulse could have a distinctive evolution trajectory because its top is flatter than the Gaussian and hyperbolic secant pulses. It requires a higher peak power to reshape the center region of temporal pulse evolve to the PP. Although the evolution of the super-Gaussian pulse into the PP was reported [17], it is still worth investigating the evolution process, especially for the passive waveguide considering the loss. The process of pulse evolution to PP can be classified as two regions: transition region and asymptotic self-similar region. Transition region means that the values of peak power and pulse width are far away from the theoretical values while the asymptotic self-similar region means the values of peak power and pulse width are almost overlapping [18, 19]. It can be seen from Figs. 3(c) and 3(d) that the evolutions of the three kinds of pulses are in the transition region. We attribute this to the unoptimized parameter of input peak power, pulse width and waveguide length in our simulation [20]. However, in the passive fibers, it has been proved that the asymptotic self-similar region can be reached via the additional second segment fiber [21] or optimized initial pulse duration, chirp and energy [22]. It is envisioned that the evolution of these three kinds of pulses will eventually enter the asymptotic self-similar region after further optimization. To quantize the difference between the generated
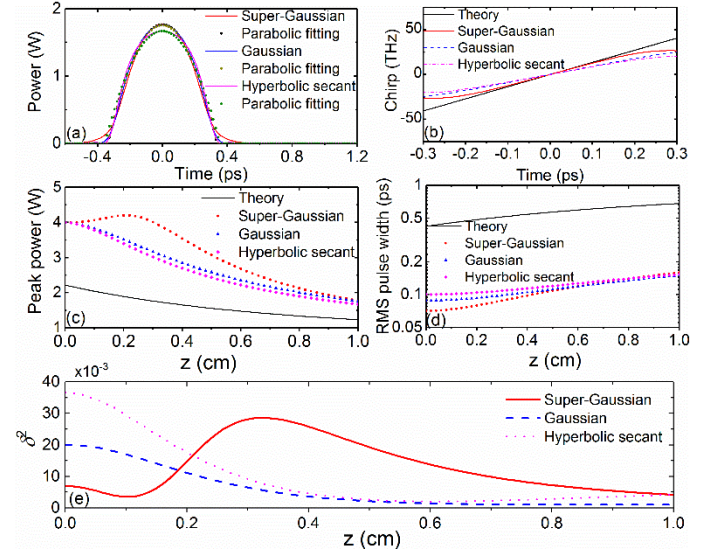

Fig. 3. (a) The temporal output at $z = 1$ cm of super-Gaussian (red solid curve), Gaussian (blue solid curve), and hyperbolic secant (pink solid curve) pulses. The black, mazarine, and green dots represent the parabolic fitting of super-Gaussian, Gaussian, and hyperbolic secant pulses, respectively. (b) The theoretical (black solid curve) and output chirps of super-Gaussian (red solid curve), Gaussian (blue dashed curve), and hyperbolic secant (pink dashed-dot curve) pulses. (c) The theoretical peak power and (d) RMS pulse width (black solid curve), along with output results of super-Gaussian (red circle dot), Gaussian (blue triangle dot), and hyperbolic secant (pink diamond dot) pulses. (e) The variations of mismatched parameter δ^2 with z for the three kinds of pulses.

pulse and PP, a mismatched parameter δ^2 is introduced as

$$\delta^2 = \frac{\int_{-\infty}^{+\infty}\left[P(t)-P_f(t)\right]^2 dt}{\int_{-\infty}^{+\infty}P^2(t)dt}, \qquad (17)$$

where $P(t)$ and $P_f(t)$ are the powers of the output pulse and parabolic fitting, respectively. The evolution of δ^2 with z is shown in Fig. 3(e). From Fig. 3(e), the initial pulse form plays an important role in the self-similar evolution. Although the

initial super-Gaussian pulse is very close to the PP, the flat-topped property makes it difficult to evolve to the PP. As a result, the complex reshaping processes accompanied by oscillating δ^2 during the propagation is observed. Although the initial δ^2 of the hyperbolic secant pulse is larger than that of Gaussian pulse, the hyperbolic secant pulse can evolve to the PP faster because of its sharper top, as shown in Fig. 3(e). However, the large value of δ^2 at the output port, especially for the super-Gaussian and hyperbolic secant pulses ($\sim 4.2\times10^{-3}$), indicates that the self-similar evolutions are in the transition region.

Next, we focus on the effects of HOD, HON, linear loss, TPA, FCA and FCD in the designed silicon waveguide taper on the evolution to PP. The HOD includes the third-order to the sixth-order dispersion, which is obtained by the Taylor expansion of GVD. The HON contains self-steepening and intra-pulse Raman scattering. The variations of all effects along the length for the proposed waveguide are considered in our simulation. The comprehensive model of an optical pulse propagating in a passive silicon waveguide taper can be described by the generalized NLSE [23, 24]

$$\frac{\partial A}{\partial z} = i\sum_{2}^{6}\frac{i^{n}\beta_{n}(z)}{n!}\frac{\partial^{n}A}{\partial t^{n}} + i\gamma(z)\left(1+\frac{i}{\omega_{0}}\frac{\partial}{\partial t}\right)A(z,t)$$
$$\times \int_{-\infty}^{t}R(t-t')\left|A(z,t')\right|^{2}dt' - \frac{1}{2}\left(\sigma_{f}+\sigma_{l}\right)A, \tag{18}$$

where $A(z, t)$ is the pulse envelope, $\beta_{n}(z)$ ($n=1, 2, 3,...6$) is the GVD coefficients at z, and $\gamma(z) = 2\pi n_{2}/[\lambda A_{\text{eff}}(z)]+i\beta_{\text{TPA}}/[2A_{\text{eff}}(z)]$, where $n_{2} = 4.5 \times 10^{-18}$ m²/W is the nonlinear refractive index and $\beta_{\text{TPA}} = 7.9 \times 10^{-12}$ m/W is the TPA coefficient. $R(t) = (1 - f_{R})\delta(t) + f_{R}h_{R}(t)$ is the nonlinear response function, where $h_{R}(t)$ is the Raman response function and $f_{R} = 0.043$ for the silicon material. The functional form of $h_{R}(t)$ can be deduced from the Raman gain spectrum [24]. The remaining terms that $\sigma_{f} = \sigma(1 + i\mu)N_{c}$ and $\sigma_{l} = 2\rho_{0}$ are the nonlinear and linear losses, respectively, where $\sigma = 1.45 \times 10^{-21}$ m² is the FCA coefficient, $\mu = 2k_{c}k_{0}/\sigma$ represents the FCD with $k_{c} = 1.35 \times 10^{-27}$ m³, N_{c} governs the free-carrier density, which is determined by the rate equation [23]

$$\frac{\partial N_{c}(z,t)}{\partial t} = \frac{\beta_{\text{TPA}}}{2h\nu_{0}}\frac{\left|A(z,t)\right|^{4}}{A_{\text{eff}}^{2}} - \frac{N_{c}(z,t)}{\tau_{c}}, \tag{19}$$

where $t_{c} \approx 3$ ns is the effective carrier lifetime. For femtosecond pulse with low repetition rate, free-carrier density $N_{c} \leq 2\beta_{\text{TPA}}P_{0}^{2}T_{0}/\left(3h\nu_{0}A_{\text{eff}}^{2}\right)$, where T_{0} is the pulse width and $T_{\text{FWHM}} = 1.665T_{0}$ is the FWHM, h is the Planck constant, ν_{0} is the frequency, and A_{eff} is the effective mode area. We use the Gaussian pulse as an example of the input pulse for PP generation. The Gaussian pulse profile is

$$A(0,t) = \sqrt{P_{0}}\exp\left[-\left(1+iC\right)\pi P_{0}^{2}t^{2}/\left(2E_{0}^{2}\right)\right], \tag{20}$$

where $P_{0} = 3.2$ W and $E_{0} = 0.88$ pJ, C is the chirp parameter.

To clearly demonstrate the influence of each effect, we consider the four cases: Case I (the ideal case), Case II (HOD and HON), Case III (HOD, HON, and linear loss), and Case IV (full model), respectively. For the four cases, C is set to be zero. In the previous work, we investigated the mid-infrared self-similar pulse compression for the four cases [25]. Here, we focus on the PP generation at wavelength 1550 nm. For the ideal case, only the interaction between GVD and nonlinearity is considered. The full model considers all the factors including the HOD, HON, linear loss, TPA, FCA, and FCD. The generalized NLSE of Eq. (18) combining with Eq. (19) is

numerically solved and the results are shown in Fig. 4. We can see that linear chirp with a positive slope is observed from Fig. 4(a). HOD and HON almost have no influence on the chirp, but the losses, especially the nonlinear loss, significantly reduce the chirp slope. The variation of δ^2 versus z is shown in Fig. 4(b). It can be seen from Fig. 4(b) that the evolution track of δ^2 for the case IV deviates from the other three cases. From 0 to 0.57 cm, the value of δ^2 for case IV is the smallest among the four cases. However, δ^2 for the other three cases gradually become smaller than that of case IV after $z = 0.57$ cm. At the end of propagation, δ^2 for the four cases are 1.36×10^{-3}, 1.36×10^{-3}, 1.48×10^{-3} and 1.83×10^{-3}. The largest δ^2 possessed by case IV indicates that the nonlinear loss induced by the TPA and FCA degrades the self-similar evolution. At the end of propagation, the peak power of temporal pulse is decreased to a so low level that the self-similar evolution cannot go on. However, the output pulse of Case IV can be well fitted by the parabola in Fig. 4(c), which indicates that the PP can be obtained in the proposed waveguide taper. Comparing with the nonlinear loss, other effects such as HOD, HON and linear loss has no obvious influence on the pulse evolution. In Fig. 4(d), the output spectra under different cases are shown. The intensity reduction caused by the linear and nonlinear losses can clearly be seen. Besides, it is easy to observe that the output spectral shapes are not parabolic. This indicates that the pulse has not completely evolved into a PP and proves that the pulse evolution is in the transition region [5, 17].
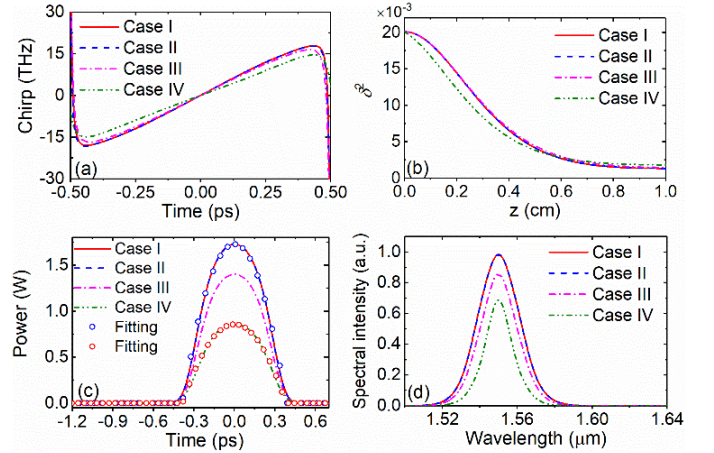

Fig. 4. (a) The output chirps for Case I (ideal case), Case II (HOD and HON), Case III (HOD, HON, and linear loss), and Case IV (full model). (b) δ^2 with respect to z. (c) Output pulses for the four cases, the blue and red hollow circles indicate the parabolic fitting for the ideal case and full model, respectively. (d) Output spectra for the four cases.

In order to investigate the effect of chirp on the PP generation, the chirp parameter C in Eq. (20) is set to be ±0.4 and ±0.8, respectively. And the outputs for the case IV in the 1-cm tapered silicon waveguide are calculated. The simulation results are shown in Fig. 5. Figure 5(a) shows the output temporal pulse and its parabolic fitting for $C = 0$. Figures 5(b) and 5(c) show the output temporal pulse and its parabolic fitting for $C = \pm0.4$ and ±0.8, respectively. By comparing Fig. 5 (a) with 5(b), the width of the output pulse at $C = -0.4$ is slightly smaller than that at $C = 0$. However, when $C = 0.4$, the width of the output pulse is slightly larger than that of $C = 0$. This is because when the chirp parameter is negative, the generated positive chirp during the self-similar evolution will be canceled and result in pulse narrowing. In contrast, the positive chirp parameter leads to pulse broadening, which is consistent with the trend of self-similar evolution. These qualitative features can be observed in Fig. 5(c) when $C = \pm0.8$.
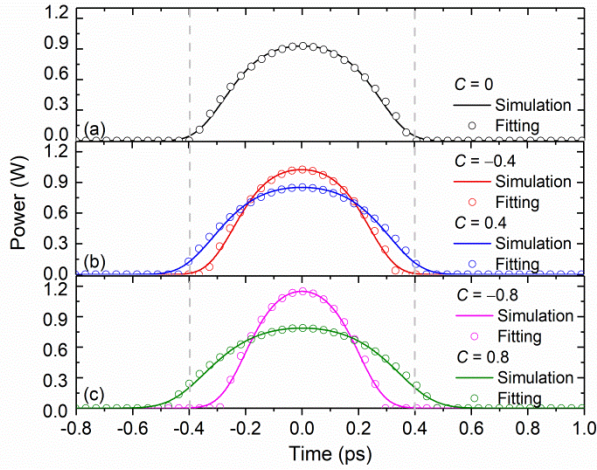
Fig. 5. The output temporal pulses (solid curves) and its parabolic fitting (hollow circles) for (a) $C = 0$ (blue), (b) $C = -0.4$ (red) and $C = 0.4$ (blue), and (c) $C = -0.8$ (pink) and $C = 0.8$ (green).

The influences of input C on the output chirp, spectrum, and δ^2 are shown in Fig. 6. It can be clearly seen from Fig. 6(a) that the negative C severely degrades the linear chirp of the PP. The larger negative C causes the chirp curve bending more severely. In contrast, positive C degrades the linear chirp much less. As in the case of a negative C, larger positive C deteriorates the linear chirp more noticeably. Figure 6(b) shows the output spectrum for different C. It can be seen that the negative C leads to the narrowing of spectrum and the positive C leads to the spectral broadening. It means that the spectral evolution for the self-similar evolution is weakened when the C is negative. The variation of δ^2 in Fig. 6(c) further reveals the influence of C on the self-similar evolution. The negative chirp accelerates the self-similar process at the initial propagation, but then the pulse deviates from self-similar evolution. While the positive C slows down the self-similar process, δ^2 is almost unchanged at the end of propagation. Therefore, negative C has a worse impact on self-similar evolution. In order to show the influence of chirp more clearly, the minimum δ^2 during the propagation and δ^2 at the output port for different C are given in Fig. 6(d). It can be seen that for all chirps, only the minimum δ^2 and output δ^2 for $C = 0$ and 0.4 are overlapped, which indicates the influence of $C = 0.4$ is the smallest. The minimum δ^2 and output δ^2 for $C = 0$ and 0.8 have different values at $z = 1$ cm, which means the general trend of self-similar evolution has not been changed. In contrast, the minimum δ^2 and output δ^2 for $C = -0.4$ and -0.8 are very different from that for $C = 0$. Thus, negative C can significantly affect the PP generation.
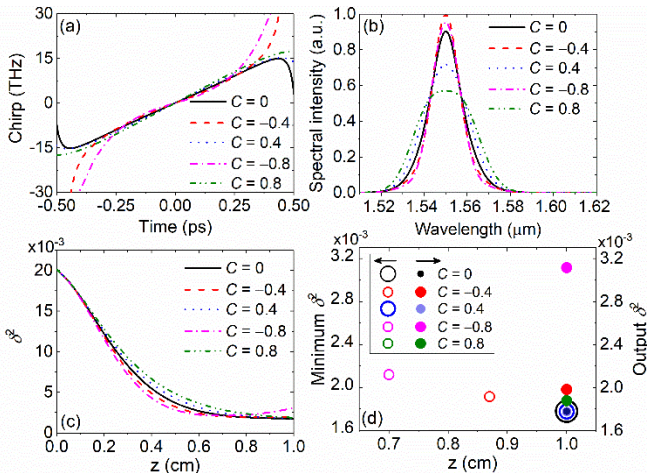

Fig. 6. (a) The output chirps, (b) spectral intensity and (c) mismatched parameter δ^2 for $C = 0$ (black curve), -0.4 (red curve), 0.4 (blue curve), -0.8 (pink curve)

and 0.8 (green curve). (d) The minimum δ^2 (hollow circle) and output δ^2 (solid circle) for $C = 0$ (black), -0.4 (red), 0.4 (blue), -0.8 (pink) and 0.8 (green).

In Fig. 7, the evolutions of temporal pulses along z are demonstrated under four cases. The white dashed arrow indicates the position where the peak power of the pulse is 2 W. it can be seen that for the four cases, the pulse widths are increased and peak powers are decreased during the propagation. In the Figs. 7(a) and 7(b), the white dashed arrows have the same location of $z = 0.55$ cm, which means the pulse evolution is not influenced by the HOD and HON. Instead, the white dashed arrow shifts to $z = 0.45$ cm in Fig. 7(c), which indicates the peak power reduction to 2 W happens earlier because of the linear loss in Case III. When the nonlinear loss participates in pulse evolution, the white dashed arrow is moved to $z = 0.3$ cm in Fig. 7(d) due to the strong influence of nonlinear loss in Case IV. However, comparing with the results reported in Refs. [24, 26], the pulse distortion induced by FCA is not observed in this work. We attributed it to the low pump peak power and ultrashort pulse used in the simulation.
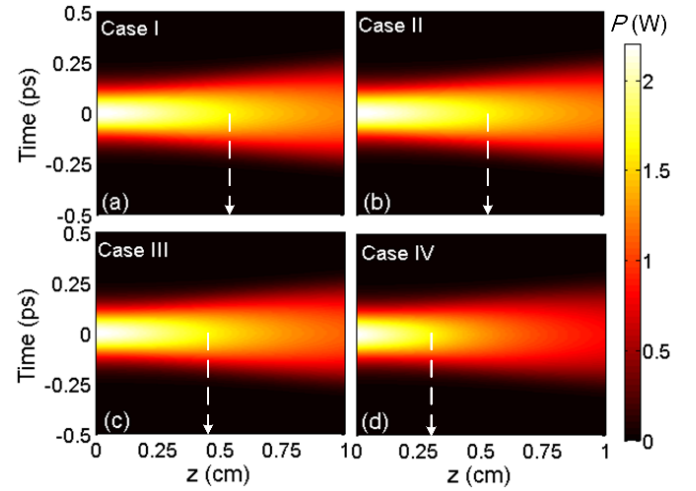

Fig. 7. The pulse evolutions along z for (a) Case I, (b) Case II, (c) Case III, and (d) Case IV.

Using the bisection method, silicon waveguide taper with different length L can be designed to investigate the impact of L on the PP generation. When L is set to be 0.5, 1, 2, and 5 cm, δ^2 under different T_{FWHM} and P_0 input can be obtained from a numerical simulation. The input T_{FWHM} and P_0 are changed from 50 to 500 fs and 1 to 20 W, respectively. The results are shown in Fig. 8 where the bright and dark areas represent the large and small values of δ^2, respectively. Figure 8 shows the processes of pulse evolution for different L. When L is 0.5 cm, the bright area is small and located at the center of upper side, as shown in Fig. 8(a). Then it enlarges and becomes more luminous when L is increased to 1 cm, as seen from Fig. 8(b). This means the degradation of generated PP is more obvious. When L is 2 cm in Fig. 8(c), the brighter area moves to the right side and becomes smaller than that in Fig. 8(b). More importantly, although the brighter area keeps moving to the right side and the size is smaller, and yet the dark area starts to lighten in Fig. 8(d). This means for $L = 5$ cm, it is difficult to obtain high-quality PP for the whole input peak power and pulse width. While the smallest values of δ^2 in Figs. 8(a) and 8(b) have the same value of 1.30×10^{-3}, it increases a litter to 1.52×10^{-3} in Figs. 8(c) and 8(d). More seriously, as L increases to 5 cm, the average value of δ^2 has obvious increment. Considering the larger linear loss of a longer waveguide, this quality degradation is reasonable. Despite longer waveguide may be in favor of PP generation in passive fibers [22], we conclude that high-quality PP can only be obtained before the self-similar evolution is broken by the

linear and nonlinear losses. Our simulation suggests that the L should be less than 5 cm if one wants to obtain high-quality within large ranges of input parameters. Although only the case of Gaussian pulse input is investigated in the model of generalized NLSE, the obtained results are also applicable for the case of super-Gaussian and hyperbolic secant pulses inputs.
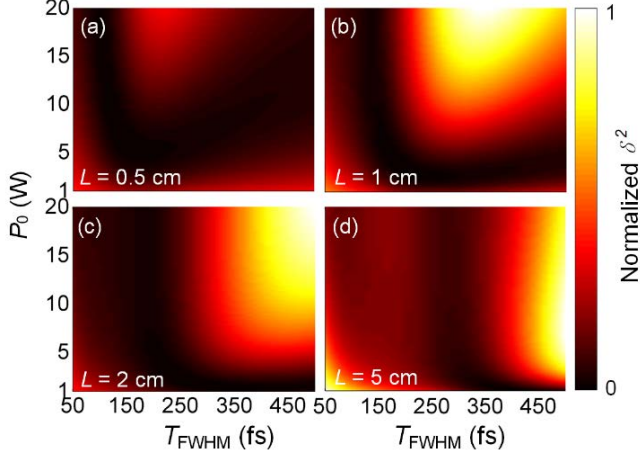

Fig. 8. The distribution of δ^2 under different inputs of T_{FWHM} and P_0 when the length of silicon waveguide taper L is designed as (a) 0.5, (b) 1, (c) 2, and (d) 5 cm, respectively.

5. Conclusions

In summary, the PP generation in a silicon waveguide taper with simultaneous variations of the GVD and nonlinearity is investigated. The pulse evolutions in the newly designed silicon are analyzed under the inputs of super-Gaussian, Gaussian and hyperbolic secant pulses. We found that under the ideal case, all kinds of pulses can evolve to PP and the evolution stay in the transition region. When the HOD, HON, linear loss, TPA, FCA, and FCD are considered, PP can still be obtained in the designed silicon waveguide taper. However, the chirp, especially the negative chirp degrades the self-similar evolution severely. Further investigation shows that for the 1-cm silicon waveguide taper, losses play important roles in the peak power reduction. However, the quality of generated PP is almost uninfluenced by the losses. This situation changed when the silicon waveguide tapers with different length are used, high-quality PP is more easily obtained in a shorter silicon waveguide taper in which the detrimental influence caused by losses are not so obvious. Besides, the PP generation is sensitive to the input pulse width and peak power. Larger range of input parameters for high-quality PP generation can be obtained in a shorter waveguide. Our research is expected to have important applications in on-chip optical pulse shaping, pulse compression and signal processing.

6. Acknowledgments

References

[1] D. Anderson, M. Desaix, M. Karlsson, M. Lisak, and M. Quiroga-Teixeiro, Wave-breaking-free pulses in nonlinear-optical fibers, J. Opt. Soc. Am. B 10 (1993) 1185-1190.
[2] Z. Liu, Z. M. Ziegler, L. G. Wright and F. W. Wise, Megawatt peak power from a Mamyshev oscillator, Optica 4 (2017) 649-654.
[3] H. Liu, Z. Liu, E. S. Lamb, and F. Wise, Self-similar erbium-doped fiber laser with large normal dispersion, Opt. Lett. 39 (2014) 1019-1021.
[4] M. Fermann, V. Kruglov, B. Thomsen, J. Dudley, and J. Harvey, Self-similar propagation and amplification of parabolic pulses in optical fibers, Phys. Rev. Lett. 84 (2000) 6010-6013.
[5] V. I. Kruglov and J. D. Harvey, Asymptotically exact parabolic solutions of the generalized nonlinear schrödinger equation with varying parameters, J. Opt. Soc. Am. B 23 (2006) 2541-2550.
[6] T. Hirooka and M. Nakazawa, Parabolic pulse generation by use of a dispersion-decreasing fiber with normal group-velocity dispersion, Opt. Lett. 29 (2004) 498-500.
[7] A. Barh, S. Ghosh, R. K. Varshney, and B. P. Pal, A tapered chalcogenide microstructured optical fiber for mid-IR parabolic pulse generation: design and performance study, IEEE J. Sel. Top. Quantum Electron. 20 (2014) 590-596.
[8] S. Lavdas, J. B. Driscoll, H. Jiang, R. R. Grote, R. M. Osgood, and N. C. Panoiu, Generation of parabolic similaritons in tapered silicon photonic wires: comparison of pulse dynamics at telecom and mid-infrared wavelengths, Opt. Lett. 38 (2013) 3953-3956.
[9] C. Mei, F. Li, J. Yuan, Z. Kang, X. Zhang, B. Yan, X. Sang, Q. Wu, X. Zhou, K. Zhong et al., Comprehensive analysis of passive generation of parabolic similaritons in tapered hydrogenated amorphous silicon photonic wires, Sci. Rep. 7 (2017), 3814-1-14.
[10] V. Kruglov, A. Peacock, J. Harvey, and J. Dudley, Self-similar propagation of parabolic pulses in normal-dispersion fiber amplifiers, J. Opt. Soc. Am. B 19 (2002) 461-469.
[11] Govind P. Agrawal, Nonlinear fiber optics, 2000
[12] K. Bergman, L. P. Carloni, A. Biberman, J. Chan, and G. Hendry, Photonic network-on-chip design, 2014.
[13] G. Li, J. Yao, H. Thacker, A. Mekis, X. Zheng, I. Shubin, Y. Luo, J.-H. Lee, K. Raj, J. E. Cunningham, and A.V. Krishnamoorthy, Ultralow-loss, high-density SOI optical waveguide routing for macrochip interconnects, Opt. Express 20 (2012) 12035–12039.
[14] P. Dong, W. Qian, S. Liao, H. Liang, C.-C. Kung, N.-N. Feng, R. Shafiiha, J. Fong, D. Feng, A. V. Krishnamoorthy, and M. Asghari, Low loss shallow-ridge silicon waveguides, Opt. Express 18 (2010) 14474–14479.
[15] M. Borselli, T. Johnson, and O. Painter, Beyond the Rayleigh scattering limit in high-Q silicon microdisks: theory and experiment, Opt. Express 13 (2005) 1515–1530.
[16] D. Marcuse, Pulse distortion in single-mode fibers, Appl. Opt. 19 (1980) 1653-1660.
[17] C. Finot, L. Provost, P. Petropoulos, and D. J. Richardson, Parabolic pulse generation through passive nonlinear pulse reshaping in a normally dispersive two segment fiber device, Opt. Express 15 (2006) 852-864
[18] C. Finot, Guy Millot, and J. Dudley, Asymptotic characteristics of parabolic similariton pulses in optical fiber amplifiers, Opt. Lett. 29 2004 2533-2535.
[19] C. Billet, J. M. Dudley, N. Joly, and J. C. Knight, Intermediate asymptotic evolution and photonic bandgap fiber compression of optical similaritons around 1550 nm, Opt. Express 13 (2005) 3236-3241.
[20] C. Finot, B. Kibler, L. Provost, and S. Wabnitz, Beneficial impact of wave-breaking for coherent continuum formation in normally dispersive nonlinear fibers, J. Opt. Soc. Am B 25 (2008) 1938-1948.
[21] C. Finot, F. Parmigiani, P. Petropoulos, and D. J. Richardson, Parabolic pulse evolution in normally dispersive fiber amplifiers preceding the similariton formation regime, Opt. Express 14 (2006) 3161-3170.
[22] I. A. Sukhoivanov, S. O. Iakushev, O. V. Shulika, A. Díez, and M. Andrés, Femtosecond parabolic pulse shaping in normally dispersive optical fibers, Optics express, 21 (2013) 17769-17785.
[23] L. Yin and G. P. Agrawal, Impact of two-photon absorption on self-phase modulation in silicon waveguides, Opt. Lett. 32 (2007) 2031-2033.
[24] L. Yin, Q. Lin, and G. P. Agrawal, Soliton fission and supercontinuum generation in silicon waveguides, Opt. Lett. 32 (2007) 391-393.
[25] J. Yuan, J. Chen, F. Li, C. Mei, Z. Kang, X. Zhang, Y. Xu, B. Yan, X. Sang, Q. Wu, X. Zhou, K. Zhong, K. Wang, C. Yu, G. Farrell, and P. K. A. Wai, Mid-infrared self-similar compression of picosecond pulse in an inversely tapered silicon ridge waveguide, Opt. Express 25 (2017) 33439-33450.
[26] A. Peacock and N. Healy, Parabolic pulse generation in tapered silicon fibers, Opt. Lett. 35 (2010) 1780-1782.